Tumbling of long flexible fibers in isotropic turbulence

Hugo Poncelet* and Gautier Verhille†
Aix Marseille Université, CNRS, Centrale Méditérranée, IRPHE, F-13384 Marseille, France

(Received 13 May 2025; accepted 13 January 2026; published xxxxxxxxxx)

In this study, we experimentally investigate the rotational dynamics of flexible fibers in homogeneous and isotropic turbulence. Three high-speed cameras are used to determine and track the three-dimensional conformation of the fibers. The rotational dynamics is characterized here by both the rotation of the end-to-end vector and the rotation of the eigenframe of the deformed fibers. We observe an increase of the rotation rate when the flexibility of the fiber is increased. To model this increase, we propose a scaling law for the evolution of the mean curvature, which depends on the mechanical properties of the fiber and the properties of turbulence. This model extends the one proposed by C. Brouzet *et al.* [Phys. Rev. Fluids **6**, 024601 (2021)] for relatively stiff fibers. The evolution of the curvature is then used to model the mean shape of a flexible fiber, which determines its rotation rate. Our model is in very good agreement with our experimental measurements as long as the mean conformation can be considered as planar—so for moderately flexible fibers.

DOI: 10.1103/d7xr-8bqk

I. INTRODUCTION

The rotation of complex shape particles such as fibers, disks, and chiral particles in turbulent flow has received more and more attention since the early 2010s. These works have been motivated by both fundamental research and more applied aspects. For instance, in the papermaking industry, the transport of fibers in flows is ubiquitous [1]. In environmental sciences, the modeling of the transport of microplastics in the ocean requires a better understanding of the advection of particles with complex shapes and various sizes [2,3]. From a fundamental point of view, the rotational dynamics of complex shape particles smaller than the Kolmogorov length depends on their orientation within the gradient of the velocity field [4]. For axisymmetric rigid ellipsoids, the rotation can be decomposed into two motions: the tumbling, corresponding to the rotation of the axis of symmetry, and the spinning, corresponding to the rotation around this axis. The preferential alignment of fibers (respectively, disk) smaller than the Kolmogorov length leads to a higher spinning rate (respectively, tumbling rate) than tumbling rate (respectively, spinning rate). In 2014, Parsa and Voth [5] investigated the tumbling rate Ω_T of nearly neutrally buoyant fibers whose length L is in the inertial range of turbulence, and highlighted that it scales as $\langle \Omega_T \Omega_T \rangle / (\langle \varepsilon \rangle / \nu) \tau_k^2 = 108 C_2 / 35 (L/\eta_k)^{-4/3}$, where $\tau_k = (\nu/\varepsilon)^{1/2}$ and $\eta_k = (\nu^3/\varepsilon)^{1/4}$ are the Kolmogorov time and length, respectively. Here, ε is the turbulent dissipation rate per unit mass, ν the fluid's kinematic viscosity, and C_2 a Kolmogorov constant. This work has been extended to the spinning of nearly neutrally buoyant rigid rods by Oehmke *et al.* [6]. They showed that, when the diameter of the fiber is larger than the Kolmogorov length, the spinning rate Ω_S follows a similar trend: $\langle \Omega_S \Omega_S \rangle \tau_k^2 \propto (d/\eta_k)^{-4/3}$ with a correction factor that depends on the ratio of the fiber length to the correlation length of the vortex filament. These

*Contact author: hugo.poncelet@univ-amu.fr
†Contact author: gautier.verhille@cnrs.fr

 ©2026 American Physical Society

studies highlighted that, for nearly neutrally buoyant fibers whose length L is longer than $\sim 10\eta_k$, both tumbling and spinning are related to the transverse structure function. Brizzolara *et al.* [7] confirmed this point and showed experimentally and numerically that the two-points statistics of the turbulence can be recovered by measuring the tumbling rate of the two extremities of the fiber. More recently, Alipour *et al.* [8] and Giurgiu *et al.* [9] focused on the rotation of bent fibers in turbulent channel flows. The specific shape of the particles allows them to measure both their spinning and their tumbling rates. They found that an increase of the curvature leads to an increase of the rotation rates for relatively short fibers ($L \simeq 2.8\eta_k$) [8], and that the spinning rate is in good agreement with numerical predictions for short fibers [9].

For slender particles the deformations induced by the turbulent fluctuations may become important and impact their dynamics. By assuming a viscous forcing proportional to the slip velocity $\boldsymbol{u} - \partial_t \boldsymbol{X}$, the deformations of a homogeneous fiber are described by the Euler-Bernoulli equation:

$$\sigma \partial_{tt} \boldsymbol{X} + \eta \partial_t \boldsymbol{X} - \partial_s (T \partial_s \boldsymbol{X}) + EI \partial_s^4 \boldsymbol{X} = \eta \boldsymbol{u}, \tag{1}$$

where $\boldsymbol{X}$ is the position of one point of the fiber, t the time, s the curvilinear coordinate, $\sigma = \rho S$ the linear density with S the cross section of the fiber, η the resistance tensor, which will be assumed as isotropic here, $T = \int f_\parallel \mathrm{d}s + EI|\partial_{ss}\boldsymbol{X}|^2$ the tension term with $f_\parallel$ the linear tangential force, E the Young's modulus of the fiber, and I its quadratic moment of area ($I = \pi d^4/64$ for a cylindrical fiber of diameter d). In this study, the deformations are overdamped, meaning that the inertial term $\sigma \partial_{tt} \boldsymbol{X}$ is negligible compared to the viscous term $\eta \partial_t \boldsymbol{X}$. Two important length scales have been identified in this regime for flexible fibers [10]. The first one characterizes the onset of the deformation and is called the linear elastic length ℓ_e, first introduced by Brouzet *et al.* [11]:

$$\ell_e \sim \frac{(EI)^{1/4}}{(\rho \eta \varepsilon)^{1/8}}. \tag{2}$$

This length scale has been interpreted as a balance between the turbulent power $\mathcal{P}_{\text{turb}}$ and the bending power $\mathcal{P}_{\text{el}}$ in a stationary regime [11]. For fibers smaller or of the order of ℓ_e only the first bending mode can be excited. The mean conformation of the fiber is then a U shape. The mean curvature $\bar{\kappa}$ has been shown to increase as $\bar{\kappa} L \sim (L/\ell_e)^4$ [12]. The second characteristic length scale is called the nonlinear viscous elastic length:

$$L_v \sim \left(\frac{EI}{\eta \varepsilon^{1/3}} \right)^{3/10}, \tag{3}$$

which characterizes the transition between the linear and the nonlinear regimes of deformation, as shown by the evolution of the maximal curvature of the fiber [13]. These two length scales are related to each other through the relation

$$\frac{L_v}{\ell_e} \sim \left(\frac{\ell_e}{\eta_k} \right)^{1/5}. \tag{4}$$

In this study, $\ell_e \gg \eta_k$, i.e., both regimes of deformations can be observed. In the nonlinear regime ($L \gg L_v$), the conformation of the fiber is expected to be fully three-dimensional (3D). It has been shown that, contrary to the maximal curvature, the mean curvature decreases with the fiber length and is smaller at the center of the fibers than close to the extremity due to the spatial correlation of the flow and the fiber inextensibility [14]. In the underdamped regime, an equivalent length scale has been identified and corresponds to the length above which the fiber deformations are enslaved to turbulent fluctuations [15].

This article is focused on the evolution of the rotation rate of flexible fibers when the fiber length is increased from $L \sim \ell_e$ to $L \sim 20 L_v$ covering the different regimes of deformation that have been identified. The article is structured as follows. The experimental setup and the fiber properties are detailed in Sec. II. The 3D reconstruction and tracking algorithms are presented in Sec. III. Finally, our results and their modeling are presented in Sec. IV before the conclusion.

TABLE I. This table gives the different scales of the flow: the turbulent dissipation rate ε, the Kolmogorov time and length scales τ_k and η_k, respectively, the integral length scale $L_I = U_{\rm rms}^3/\varepsilon$, and the Taylor Reynolds number $\mathrm{Re}_\lambda = \lambda U_{\rm rms}/\nu$ associated to the Taylor microscale $\lambda = U_{\rm rms}\sqrt{15\nu/\varepsilon}$.

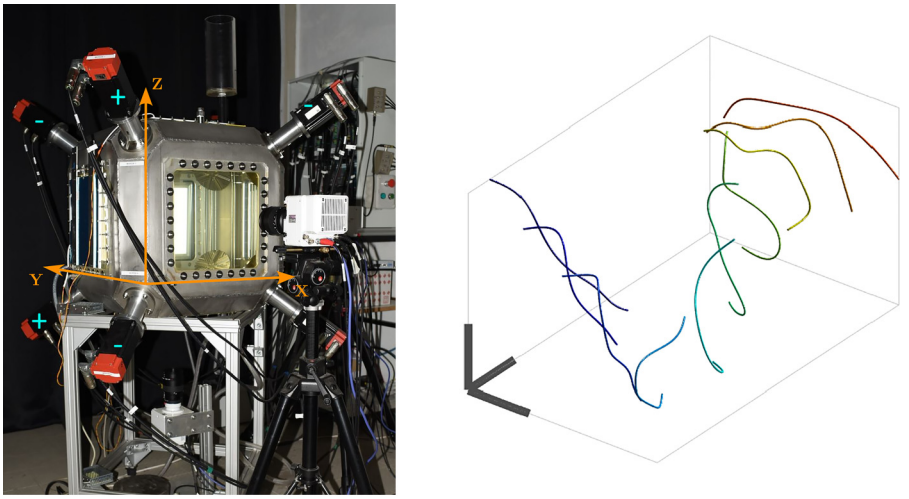
ε (m^2 s^{-3})	η_k (μm)	τ_k (ms)	Re_λ	$U_{\rm rms}$ (m s^{-1})	L_I (mm)
(4.5×10^{-2})–1.24	30–69	0.89–4.7	400–820	0.12–0.41	42–55

II. EXPERIMENTAL SETUP

A. The flow

The experiments are made in a cubic tank having a side length of 60 cm, filled with degassed water to avoid the apparition of bubbles. The flow is generated by the rotation of eight impellers, whose diameter is 17 cm, fitted with eight straight blades (5 mm wide and thick). Each of them is located at one corner of the tank and driven independently by a 1.5-kW brushless motor. In this study, all the impellers rotate at the same frequency $f_{\rm rot}$, varying from 6 to 18 Hz, but in opposite directions compared to their closest neighbors. At the center of the tank, the flow is close to a homogeneous and isotropic turbulence and has already been used in several other studies [6,16,17]. The main quantities measured using particle image velocimetry in the center of the tank are given in Table I.

Each face of the cube is equipped with a plane transparent polymethyl metacrylate plate that allows the lighting by using light-emitting diode panels as backlights, and the visualization of the particles. Three high-speed Phantom VEO 710 cameras, having their axis perpendicular to the window, are used to simultaneously image the fibers within a volume of reconstruction of nearly $8 \times 8 \times 8$ cm^3 located at the center of the tank. The frame rate $f_{\rm acq}$ of the cameras varies with the rotation rate of the impellers as $f_{\rm acq} = 200 f_{\rm rot} \in [1200; 3600]$ fps. The experimental setup is shown in Fig. 1(a). All the results presented in this article have been obtained in a statistically stationary



(a) (b)

FIG. 1. (a) Photo of the experimental setup. The blue symbols "+" and "−" show the polarity of the motors. The laboratory frame axes are in orange (the origin is located at the center of the tank). (b) A typical trajectory of a reconstructed fiber $[(L, d, E) = (15\ \text{mm}, 130\ \mu\text{m}, 5\ \text{kPa})$ and $f_{\rm rot} = 18$ Hz]. The color codes the time (from blue to red). The time lag between two snapshots is $\delta t \simeq 8.3$ ms. The three 5-mm-long, thick, dark lines at the bottom left scale the size of the box.

TABLE II. Mechanical properties and deformability ratios L/L_v and L/ℓ_e of the fibers. In this study a set of fibers will always be labeled as (L, d, E) in (mm, μm, kPa). For instance, the second type of fiber is labeled (10, 400, 70). The lengths ℓ_e and L_v are, respectively, the linear elastic length and the nonlinear viscous-elastic length, defined respectively in (2) and (3).

$L \pm 0.5$ (mm)	$d \pm 10$ (μm)	E (kPa)	$\Lambda = L/d$	L/ℓ_e	L/L_v	Plot color	Type
20	990	2000	20	0.77–1.2	0.24–0.33	●	I
10	400	70	25	2.2–3.4	0.96–1.3	●	II
20	990	5	20	3.5–5.2	1.4–2.0	●	III
15	400	70	37	3.3–5.0	1.4–2.0	●	IV
20	400	70	50	4.4–6.7	1.9–2.7	●	V
15	130	70	115	10–15	5.5–7.7	●	VI
15	130	5	115	20–30	12–17	●	VII

regime. To reach this regime, the measurements have been done approximately after 15 s, so at least 75 integral time scales after all the impellers have reached their final rotation rate. Note that some measurements have been done after 1 min without any modification of the results.

B. The fibers

The fibers are molded in the laboratory using silicone to tune at wish their lengths L, diameters d, and Young's moduli E. Three kinds of silicone from Esprit Composite have been used to vary the Young's modulus: R1 55 ($E \simeq 2$ MPa), Skin FX 10 ($E \simeq 70$ kPa), and Skin FX 00-20 ($E \simeq 5$ kPa). The manufacturing process is the following: parts A and B and a silicone dye (used to make the fiber opaque) are mixed together. The mixture is then degassed to avoid the apparition of bubbles. It is then injected into needles, used as molds that fix the fiber diameter. After curing, the fibers are finally cut at the desired length. The mechanical properties of the fibers used in this study are given in Table II.

III. POSTPROCESSING: FROM 3D RECONSTRUCTION TO THE INDIVIDUAL TRACKING OF THE PARTICLES

A. 3D reconstruction

In this section we explain the principles of the 3D reconstruction of the fibers from the simultaneous images taken by the three high-speed cameras. The first step is to determine the two-dimensional (2D) coordinates of the projected fibers on each image. To do so, the image is first removed from the background on each frame to make the fibers brighter. Then, a threshold is applied to get the list of pixels corresponding to particles seen by the cameras. Note that several fibers are usually imaged simultaneously by the cameras.

The second step is to compute the 3D coordinates of the fiber from the list of pixels. This requires a model for the camera to convert the 2D coordinates on the images to the 3D coordinates in the laboratory frame. The model used here is the pinhole model, which assumes that all the rays of light propagate in straight lines from the object to the sensor by going through the pinhole [18]. With this model, there is a linear relation between the 2D image coordinates $\boldsymbol{q} = (u, v)^\intercal$ and the 3D coordinates in the laboratory frame $\boldsymbol{Q} = (X, Y, Z)^\intercal$ ($^\intercal$ is the transpose symbol) using homogeneous coordinates [19]:

$$\boldsymbol{q}_h \propto \mathbb{P}\boldsymbol{Q}_h, \tag{5}$$

where $\boldsymbol{Q}_h \propto (X, Y, Z, 1)^\intercal$ and $\boldsymbol{q}_h \propto (u, v, 1)^\intercal$ are the coordinates of the points expressed in homogeneous coordinates and $\mathbb{P}$ is the projection matrix, which characterizes the camera. This projection matrix depends on 11 parameters: 6 extrinsic, corresponding to the position and orientation of

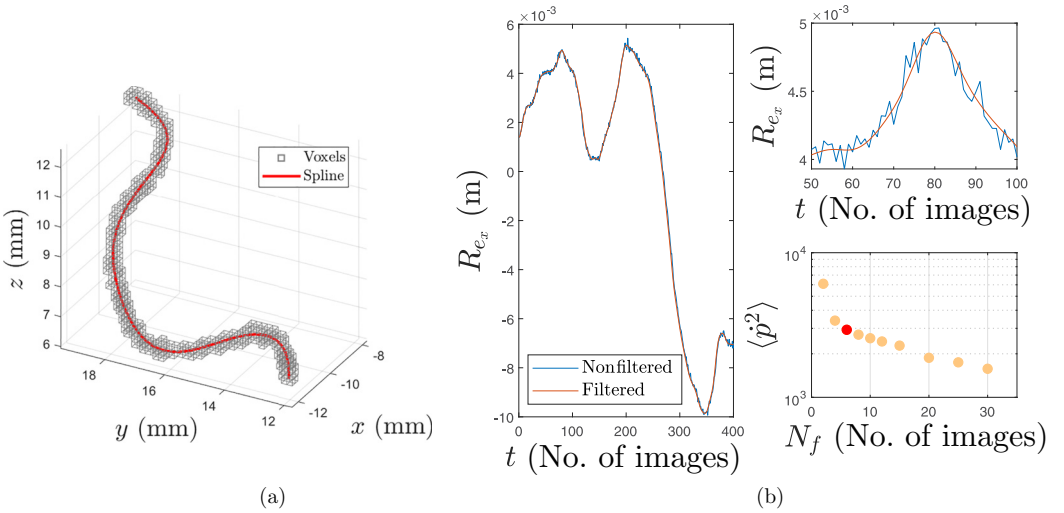


FIG. 2. (a) Example of a 3D reconstruction. The spline function (in red) is computed from the positions of the voxels (gray cubes). (b) Center: Superposition of the filtered and nonfiltered end-to-end vector projection on the x axis R_{e_x}. (b) Top right: zoom on a maximum of the x coordinate of the end-to-end vector to help see the difference between the filtered and nonfiltered data. (b) Bottom right: Evolution of the variance of the tumbling rate $\langle \dot{p}^2 \rangle$ (described later) as a function of the filtration parameter N_f. From $N_f = 6$ (red dot), the decrease becomes slower, meaning that the noise is already filtered. $N_f = 6$ is the filtration parameter used in this study. All the graphics on that figure have been made with data from fiber type VII (most flexible, see Table II).

the camera in the laboratory frame, and 5 intrinsic, containing the focal length in terms of pixels dimensions α_x and α_y, the coordinates of the projection of the pinhole onto the image plane x_0 and y_0, and the skewness μ_s. The three projection matrices $\mathbb{P}_i$ are determined thanks to a prior calibration. Each camera is calibrated independently by imaging a sphere at known positions in space. The projection matrices are then determined using the relation $\boldsymbol{q}_h \times \mathbb{P}\boldsymbol{Q}_h = 0$ for coincident points using homogeneous coordinates. By taking advantage that the projection of the center of the sphere corresponds to the center of the projected disk for all views, one can solve this relation with $\mathbb{P}$ as the only unknown. The projection matrices are then optimized by minimizing the distance between the coordinates of the projection of the sphere center and those measured on the images.

The determination of the 3D conformation of the fiber is a two-step process. The first step is based on the shape from the silhouette method, also known as the convex hull method [20]. In this method the volume of reconstruction is subdivided into voxels, and only the ones whose projections belong to a flexible fiber onto the three cameras are stored. In this study, the voxels are cubes of side length $l_{\text{res}} = 2$ mm initially. The resolution is then refined to $l_{\text{res}} = 0.2$ mm around the reconstructed objects to increase the precision of the reconstruction. A two-stage process for the voxelization has been chosen to minimize the allocated memory needed for the reconstruction. The second step of the reconstruction process corresponds to the determination of the centerline of the fiber from the set of voxels. The coordinates of the centerline are defined as $\boldsymbol{X}(s),\ s \in [0, L]$. In this study, the centerline is determined by fitting a spline function to the set of voxels by minimizing the distance between all the points of the spline and the voxels. Splines are parametric curves computed as a series of polynomial functions, of degree 4 in our case to ensure the continuity of the derivative of the curvature. Their shape is determined by control points (more details are given in [21,22]). Increasing the number of control points allows one to fit higher deformations. In practice, the voxels are fitted using 10 control points. Finally, the length of each spline L_{spl} is computed, and if $0.9 < L_{\text{spl}}/L_f < 1.1$, the reconstruction is considered as valid. An example of the voxels and the spline function computed from their coordinates is shown in Fig. 2(a).

B. Individual tracking of particles

Once the centerline has been determined, it remains to track its evolution with time. The concentration of fibers being low, only the distance between fibers have been considered to implement the trajectory. In our process of reconstruction, the distance between two consecutive sets of voxels is considered, instead of the splines. It allowed us to test several methods to fit the voxels without having to compute the tracking stages several times. If several fibers satisfy the distance criterion at the same time step, only the one with the smallest distance between all the voxels is considered. The trajectories that are considered too short (less than 50 images) are discarded.

To characterize the influence of the deformations on the fiber dynamics, we will consider both the rotations of the end-to-end vector $\boldsymbol{R_e}$ linking the two extremities of the fiber, and of the eigenframe of the fiber, defined by the eigenvectors of the moment of inertia tensor (described later). As for our previous study on rigid fibers [6], the temporal evolutions of these quantities are filtered using spline to compute their derivatives [see Fig. 2(b)]. The number of control points $N_{\mathrm{ctrl}}^{\mathrm{f}}$ is defined as the closest integer of $(t_f - t_0)/N_{\mathrm{f}}$, where t_0 and t_f are, respectively, the initial and final time of the trajectory, and N_{f} is a constant related to the cut-off frequency of the filter. For this study, $N_{\mathrm{f}} = 6$ images has been chosen by analyzing the evolution of the variance of the tumbling rate $\langle \dot{p}^2 \rangle$ as a function of N_{f}; see the evolution of the variance of the tumbling rate for fibers of type VII on Fig. 2(b) (similar evolutions have been observed for the other fibers). The exact value of N_{f} does not qualitatively impact the evolution of the results presented here as long as it remains of the order of 6. The filtered trajectories smaller than 70 time steps are discarded, and the first and last N_{f} points are removed to avoid the effects of the boundaries of the trajectory.

C. Validation of the 3D reconstruction algorithm: the end-to-end vector

To validate the reconstruction algorithm, the statistics of the norm of the end-to-end vector R_e measured experimentally are compared with the results from the literature [11,14,23]. The end-to-end vector is defined as

$$\boldsymbol{R_e} = \boldsymbol{X}(L) - \boldsymbol{X}(0), \tag{6}$$

where $\boldsymbol{X}(L)$ and $\boldsymbol{X}(0)$ are the positions of the extremities of the centerline. The evolution of $\langle R_e \rangle^2 / L^2$, where $\langle \cdot \rangle$ corresponds to a time and ensemble average as a function of the fiber length normalized by the linear elastic length L/ℓ_e is shown in Fig. 3(a). Our results are compared with the numerical data from Sulaiman *et al.* [23] and predictions from the wormlike chain model [24]. In this model the tangent vector $\boldsymbol{t}(s)$ is assumed to decorrelate exponentially:

$$\langle \boldsymbol{t}(s)\boldsymbol{t}(s+\ell) \rangle = \exp(-\ell/\ell_p), \tag{7}$$

where ℓ_p is called the persistence length. With this relation, one can easily show

$$\frac{\langle R_e^2 \rangle}{L^2} = 2\frac{\ell_p}{L} - 2\left(\frac{\ell_p}{L}\right)^2 \left[1 - \exp\left(-\frac{L}{\ell_p}\right)\right], \tag{8}$$

where L is the polymer (here the fiber) length at rest. This model has been shown to well fit the evolution of the norm of the end-to-end vector of a flexible fiber in turbulence, ℓ_p being a function of L/ℓ_e [11]. In Fig. 3(a), the global trends of our datasets and those from the literature are in good agreement up to $L/\ell_e \simeq 7$. The fact that R_e are slightly higher in the experiments than in the numerical simulations might be due to a Reynolds number dependence. Indeed, there is a small change in the numerical simulations when passing from $\mathrm{Re}_\lambda = 51$ to 97. The lowest Reynolds number tested here is $\mathrm{Re}_\lambda = 400$. Further investigations are needed to understand this point. For fibers longer than $7\ell_e$, the decrease of the norm of the end-to-end vector is slower in our measurements. This relative stiffening is compatible with the results of Gay *et al.* [14]. It has

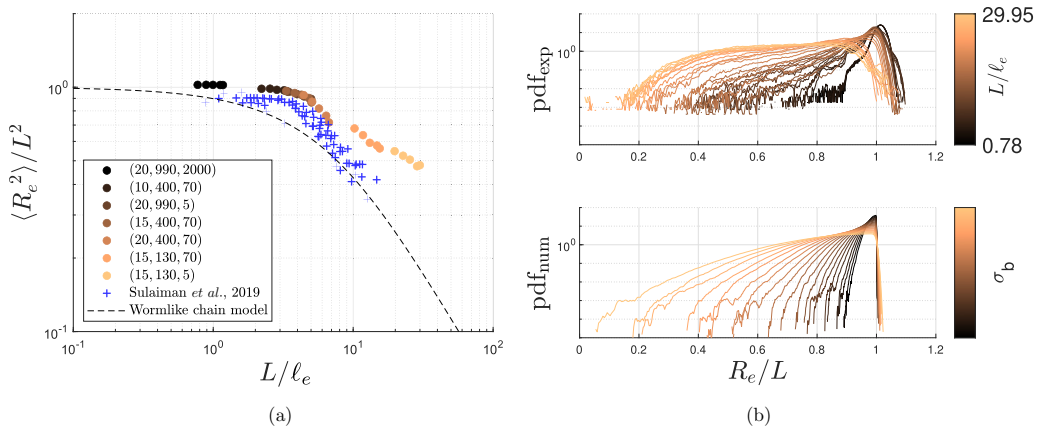


FIG. 3. (a) Evolution of the mean of the normalized end-to-end distance as a function of the fiber length L normalized by the elastic length ℓ_e (2). The results are compared with the numerical results of Sulaiman *et al.* [23] (blue cross) and with the wormlike chain model proposed in Brouzet *et al.* [11] (dashed line). The color of the symbol codes the ratio L/L_v, i.e., the fiber flexibility (see Table II), from low value (dark) to high value (bright). (b) Evolution of the pdf of the end-to-end distance, normalized by L. The figure on the top shows the experimental data, and the one at the bottom the numerical data from the toy model detailed in Eq. (11).

been related to the fiber inextensibility and to an additional viscous dissipation during the fiber reconfiguration.

The probability distribution functions (pdfs) of the norm of the end-to-end vector for different deformability ratios are shown at the top of Fig. 3(b). The distributions are negatively skewed. The qualitative evolution of the shape of the pdf can be easily reproduced with a simple model of a flexible dumbbell, i.e., two beads linked by a spring of stiffness k. By noticing that the stretching of the fiber is much harder than the bending, the stiffness of the spring k should be different for bending (compression of the dumbbell) and stretching (extension of the dumbbell) and should scale as [25]

$$k_{\mathrm{bend}} \sim \frac{EI}{L^3} \text{ for bending } (R_e < L), \tag{9a}$$

$$k_{\mathrm{str}} \sim \frac{Ed^2}{L} \text{ for stretching } (R_e > L) \tag{9b}$$

for a straight rod of length L at equilibrium, with a circular cross section of diameter d. The ratio of the two stiffnesses scales as $k_{\mathrm{bend}}/k_{\mathrm{str}} \sim (d/L)^2 \ll 1$ for long rods. This model is valid for fibers close to the threshold of deformation, for which only the first bending mode is excited. Within this toy model, the dynamic of the length of the dumbbell R_{e_d} is given by a Langevin equation:

$$m\ddot{R}_{e_d} = \eta d\big(U_L - \dot{R}_{e_d}\big) - 2k\big(R_{e_d} - L\big), \tag{10}$$

where m is the mass of the beads and η the fluid dynamic viscosity. In the overdamped regime (inertialess dumbbell), the Langevin equation can be rewritten as

$$\dot{R}_{e_d} + \frac{2k}{\eta d} R_{e_d} = U_L + \frac{2k}{\eta d} L. \tag{11}$$

Here, U_L is a random noise δ correlated in time to mimic, at first order, the forcing by the turbulent fluctuations. Increasing the flexibility of the fiber can then be done by increasing the variance of the forcing σ_b or decreasing the spring stiffness. Here only the first choice has been considered. The pdf of the length of the dumbbell from this toy model are shown at the bottom right of Fig. 3(b). The evolution of these pdf exhibits a similar trend as the experimental ones: they are negatively skewed

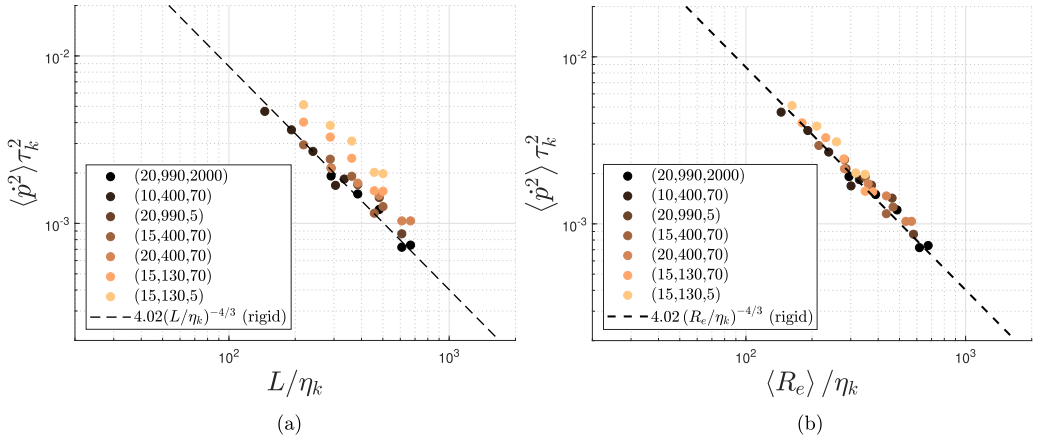


FIG. 4. (a) Evolution of the variance of the tumbling rate normalized by the Kolmogorov time τ_k, as a function of the fiber length normalized by the Kolmogorov length η_k. (b) Evolution of the tumbling rate normalized by the Kolmogorov time τ_k, as a function of the fiber end-to-end vector normalized by the Kolmogorov length η_k. For both figures, the dashed line corresponds to the evolution measured for rigid fiber [6].

and increasing the flexibility leads to a broadening of the distribution. Note that, in the experiments, a second peak appears for the most flexible cases, which is not captured by our simple model. This is probably due to the nature of the deformations, which cannot be modeled with only one mode of deformation in these cases, as we will see later.

IV. RESULTS AND DISCUSSIONS

As mentioned in the introduction, the tumbling rate of a rigid axisymmetric fiber is defined as the rotation rate of its axis of symmetry. In general, there is no axis of symmetry for a deformed fiber. The tumbling rate is then defined here as the rotation rate of the end-to-end vector $\boldsymbol{R_e}$:

$$\dot{\boldsymbol{p}} = \partial_t \boldsymbol{p} = \partial_t \left(\frac{\boldsymbol{R_e}}{R_e} \right). \tag{12}$$

This definition is equivalent to the classic definition of the tumbling rate for axisymmetric rigid fibers. The evolutions of the variance of the normalized tumbling rate $\langle \dot{p}^2 \rangle \tau_k^2$ as a function of the normalized fiber length L/η_k are shown in Fig. 4(a). If a global trend $\langle \dot{p}^2 \rangle \tau_k^2 \sim (L/\eta_k)^{-4/3}$ seems to appear, there is an important scattering of the data with an increase of the tumbling rate with the fiber flexibility. For rigid fibers, higher rotation rate corresponds to smaller length. To collapse the data, it is appealing to look for an effective length, shorter than the fiber length, which decreases when the fiber flexibility is increased. The mean norm of the end-to-end vector is a natural candidate for the effective length as it decreases when the flexibility of the fiber increases, as we saw in the previous section [see Fig. 3(a)]. The evolutions of the normalized tumbling rate as function of the mean end-to-end distance normalized by the Kolmogorov length are shown in Fig. 4(b). The collapse of the data here is better than when the fiber length L is considered [Fig. 4(a)]. Moreover, the prefactor for flexible fibers is almost equal to the one measured experimentally for rigid fibers [dashed line in Fig. 4(b)]. This suggests that an analogy can be drawn between the rotation of rigid and flexible fibers by considering the end-to-end distance as the effective length of a fiber initially straight. In the following, a more complete description of the global rotation of flexible fibers is proposed.

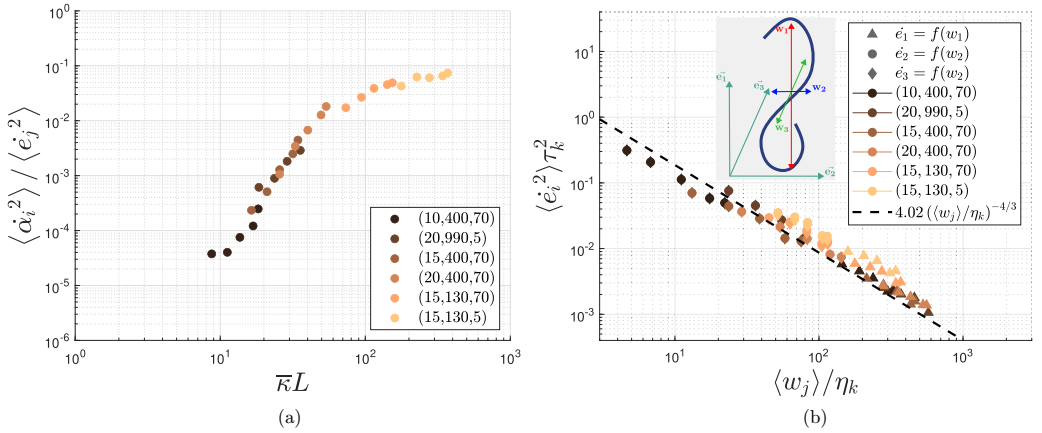


FIG. 5. (a) Evolution of the ratio of the reconfiguration rate of the eigenframe $\langle \dot{\alpha}_i^2 \rangle$ against the rotation rate of the eigenvectors $\langle \dot{e}_i^2 \rangle$, as a function of the normalized mean curvature $\overline{\kappa} L$ computed from the model (29). (b) Evolution of the normalized mean of the rotation rates of the eigenvectors $\langle \dot{e}_i^2 \rangle \tau_k^2$, as a function of the normalized mean extents $\langle w_j \rangle / \eta_k$. For the rotation of $\boldsymbol{e_1}$, the transverse extent is w_1. For the rotations of $\boldsymbol{e_{2,3}}$, only the largest transverse extent w_2 is considered. The dashed line represents the fit found by Oehmke *et al.* [6] for the tumbling of rigid fiber (by replacing the fiber length L by the transverse extent w_j). The inset is a scheme of the extents of a deformed fiber.

Following the work from Giurgiu *et al.* [9], here we use the moment of inertia tensor as a proxy for the global shape of the fiber. The moment of inertia tensor is defined as

$$\mathbb{I}_{ij} = \int \sigma \Delta_{ij} \mathrm{d}s, \tag{13}$$

where $\Delta_{ii} = \sum_{j \neq i} x_j^2$, $\Delta_{ij} = -x_i x_j$, and $\boldsymbol{x} = \boldsymbol{X} - \langle \boldsymbol{X} \rangle$ is the coordinate of a fiber point in the frame with its origin at the center of mass of the fiber. We remind one here that $\boldsymbol{X}$ is the coordinate of the centerline of the fiber computed from the 3D reconstruction process. The global rotation is then defined as the rotation of the eigenframe of the moment of inertia tensor. The eigenvectors are labeled $\boldsymbol{e_i}$. The corresponding eigenvalues λ_i are ordered as $\lambda_3 \gtrsim \lambda_2 > \lambda_1$. In the laboratory frame, the eigenvectors vary due to both the rotation of the deformed fiber and its reconfiguration. We will assume in the following that the variation of the eigenframe due to the reconfiguration is negligible. We have partially validated this assumption by looking at the evolution of the rotation rate of the end-to-end vector. Indeed, in the fiber frame, the unit vector of the end-to-end vector defined in Eq. (12) is given by

$$\boldsymbol{p} = \frac{\boldsymbol{R_e}}{R_e} = \alpha_i \boldsymbol{e}_i, \tag{14}$$

where Einstein convention is adopted. α_i are the coordinates of the vector $\boldsymbol{p}$ in the eigenframe. Hence, the rotation rate is given by

$$\langle \dot{\boldsymbol{p}} \dot{\boldsymbol{p}} \rangle = \langle \dot{\alpha}_i \dot{\alpha}_i \rangle + \langle \alpha_i \alpha_i \dot{\boldsymbol{e}}_i \dot{\boldsymbol{e}}_i \rangle + 2 \langle \alpha_i \dot{\alpha}_j \boldsymbol{e}_i \dot{\boldsymbol{e}}_j \rangle. \tag{15}$$

The first term is related to the change of conformation within the eigenframe and the second to the rotation of the eigenframe. The third term is a cross term expected to be equal to zero as $\boldsymbol{e_i} \cdot \dot{\boldsymbol{e}}_i = 0$ ($\dot{\boldsymbol{e}}_i = \Omega \times \boldsymbol{e_i}$). The ratio of the rates of reconfiguration $\langle \dot{\alpha}_i \dot{\alpha}_i \rangle$ and the rotation rate $\langle \dot{e}_i \dot{e}_i \rangle$ is shown in Fig. 5(a). For all the cases under study, the reconfiguration term is at least one order of magnitude smaller than the rotation rate term justifying our approximation. In the following, we will then assume that $\dot{e}_i$ is only due to the rotation of the eigenframe.

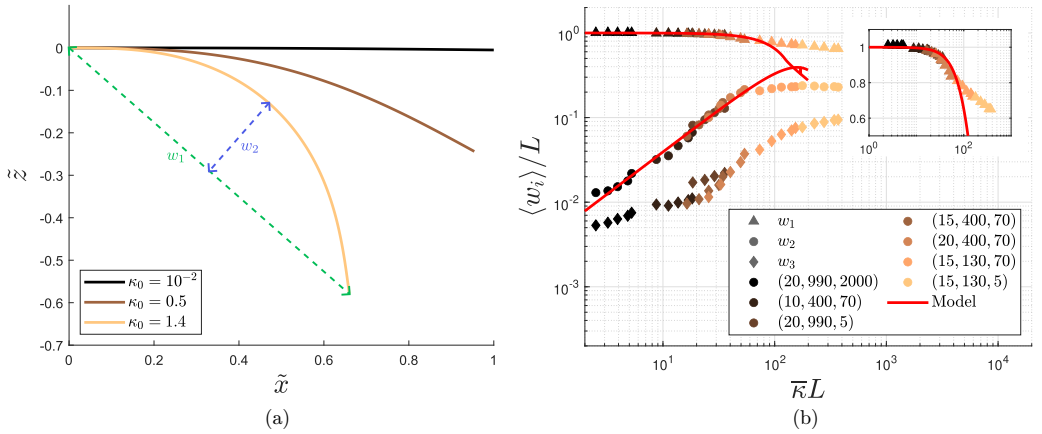


FIG. 6. (a) Example of the shapes of the fibers computed from the integration of Eq. (19) for three values of $\kappa_0 = \{10^{-2}, 0.5, 1.4\}$. $\tilde{x}$ and $\tilde{z}$ are, respectively, the x and z coordinates normalized by the fiber length L. The colors code the mean curvature (flexibility): from the straightest (black) to a more bent case (yellow). The extents $w_{1,2}$ are schematized for the most flexible case. (b) Fiber extents w_i as a function of the mean curvature model $\overline{\kappa} L$ (29). The red lines represent the mean extents obtained from the resolution of Eq. (17). The inset shows the evolution of w_1/L as a function of $\overline{\kappa} L$, in a semilogarithmic plot.

Oehmke *et al.* [6] showed that both tumbling and spinning are governed by the transverse structure function at the scale of the relevant extent of the fiber (length for tumbling and diameter for spinning). By analogy, the evolution of the rotation rate of the three eigenvectors are plotted as function of the mean extents $\langle w_i \rangle$ of the deformed fibers on Fig. 5(b), where the extents are defined as

$$w_i = \max_{\boldsymbol{x}} (\boldsymbol{x} \cdot \boldsymbol{e_i}) - \min_{\boldsymbol{x}} (\boldsymbol{x} \cdot \boldsymbol{e_i}). \tag{16}$$

Here again, the dashed line corresponds to the fit of the tumbling rate of rigid fibers proposed by Oehmke *et al.* [6]. The collapse of all the experimental points shows that, as for the tumbling and spinning of rigid fibers, the rotation rate of the eigenframe is controlled by the mean lateral extent of the fiber. Thus, the rotation rate of $\boldsymbol{e}_1$ is governed by the maximal extent $\langle w_1 \rangle$, corresponding to the fiber length in the rigid case. The rotation rates of $\boldsymbol{e}_{2,3}$ both depend on the largest lateral extent $\langle w_2 \rangle$, corresponding to the diameter for rigid fibers. Moreover, there is a quantitative agreement between the evolution of $\langle \dot{\boldsymbol{e}}_i \dot{\boldsymbol{e}}_i \rangle \tau_k^2$ for flexible fibers and the tumbling rate of rigid fibers. In this frame, the equivalent of the spinning rate of rigid fiber is the total rotation vector $\boldsymbol{\Omega}$ projected on $\boldsymbol{e_1}$. So, the rotation rates of $\boldsymbol{e}_{2,3}$ are both a combination of spinning and tumbling (the latest being $\boldsymbol{\Omega}$ projected on $\boldsymbol{e_2}$ and $\boldsymbol{e_3}$). As a consequence, the rotation rate of $\boldsymbol{e}_{2,3}$ of flexible fibers is higher than the spinning rate of straight rigid fibers (see [6]). A full understanding of this phenomenon might require a simultaneous measurement of the flow field and the fiber dynamics, as preferential alignment within vortices has been invoked to model the spinning rate of straight rigid fiber. Note that here, the data from fiber type I has been removed as the signal to noise ratio is too high due to the very low amplitude of the deformation.

The last step to model the evolution of the rotation rate of flexible fibers in turbulence is to relate the evolution of the extents to the fiber deformation. As long as w_3 is negligible [see Fig. 6(b)], the deformations can be considered as planar, and we assume they are deformed on one mode. The mean shape is then expected to be a U shape with maximal curvature at the center and zero curvature at extremities due to the boundary condition (see Gay *et al.* [14]). In that case, a first-order approximation is to model the evolution of the curvature as

$$\kappa_{\text{num}}(s) = 6 \frac{\kappa_0}{L^2} s(L - s). \tag{17}$$

The mean curvature is then

$$\overline{\kappa_{\rm num}} = \frac{1}{L}\int_0^L \kappa_{\rm num}(s)\mathrm{d}s = \kappa_0. \tag{18}$$

This model can be integrated numerically by using the relation

$$\partial_s \boldsymbol{t}(s) = \boldsymbol{\kappa}(s) \times \boldsymbol{t}(s), \tag{19}$$

where $\boldsymbol{t}$ is the unit tangent vector, and $\boldsymbol{\kappa}(s) = (0, \kappa_{\rm num}(s), 0)^\top$ is the curvature vector chosen to bend a fiber in the (xz) plane. The extents are then computed using relation (16). Three conformations with $\kappa_0 = 10^{-2}$, 0.5, or 1.4 can be seen in Fig. 6(a).

It remains now to relate κ_0 to the mean curvature of a fiber $\bar{\kappa}$, which depends on the mechanical properties of the fiber, those of the fluid and the turbulence intensity. Brouzet *et al.* [12] showed that, for short fibers ($L \lesssim \ell_e$), the mean curvature $\overline{\kappa}$ varies as $\overline{\kappa}L \sim (L/\ell_e)^4$. For very long fibers, Gay *et al.* [14] showed that the mean curvature $\bar{\kappa}$ of the fibers decreases. Considering only planar conformation of flexible fibers means that we are in between these two regimes. In both Brouzet *et al.* [12] and Gay *et al.* [14], a power budget has been used to successfully estimate the evolution of the mean curvature. We will adopt here the same approach. The power budget can be justified as follows: we consider the system made of the ensemble of the fibers immersed in a stationary, homogeneous and isotropic turbulent flow. The variation of energy of this system $\mathcal{E}$ is equal to the difference between the power injected by the turbulence into the system $\mathcal{P}_{\rm inj}$ and the dissipated power $\mathcal{P}_{\rm dis}$, i.e., the one given back by the system to the turbulence:

$$\partial_t \mathcal{E} = \mathcal{P}_{\rm inj} - \mathcal{P}_{\rm dis}. \tag{20}$$

As the system is statistically stationary,

$$\mathcal{P}_{\rm inj} = \mathcal{P}_{\rm dis}. \tag{21}$$

To derive the typical evolution of the mean curvature $\bar{\kappa}$, only scaling arguments are needed. At first order, the injected power $\mathcal{P}_{\rm inj}$ is proportional to the power of eddies of scale L, so,

$$\mathcal{P}_{\rm inj} \sim \rho L^3 \varepsilon. \tag{22}$$

For long fibers two sources of dissipation have been identified: an elastic one, $\mathcal{P}_{\rm el}$, related to the deformation, and a viscous term, $\mathcal{P}_{\rm vis}$, due to the viscous dissipation during the global reconfiguration of the fiber imposed by the local deformation and the fiber inextensibility [14]. The elastic power scales as [12]

$$\mathcal{P}_{\rm el} \sim \frac{E_{\rm el}}{\tau_b} = \frac{LEI\kappa^2}{\tau_b}, \tag{23}$$

where

$$\tau_b = \frac{\eta \kappa^{-4}}{EI} \tag{24}$$

is the typical time scale of the deformation. The viscous dissipation power has been first introduced by Gay *et al.* [14] and scales as

$$\mathcal{P}_{\rm vis} \sim \eta L u_L v_\kappa, \tag{25}$$

where $u_L \sim (\varepsilon L)^{1/3}$ is the typical velocity of eddies of size L. $v_\kappa \sim 1/\kappa\tau_b$ is the characteristic speed of evolution of the local deformation of typical size κ^{-1} evolving on the typical time scale τ_b. The ratio of these two dissipative powers is

$$\mathcal{R}_{\mathcal{P}}(L) = \frac{\mathcal{P}_{\rm el}}{\mathcal{P}_{\rm vis}} \sim \frac{\kappa^3 \ell_e^4}{\eta_k^{2/3} L^{1/3}}. \tag{26}$$

By approximating κ^{-1} by the fiber length L at the transition between the elastic dominated regime (short fibers) and the viscous dominated regime (long fibers), one finds that the critical length corresponds to the nonlinear viscous elastic length L_v. For short fibers ($L \ll L_v$), the dissipated power is mainly due to the elastic energy stored in the fiber and the mean curvature evolves as $\bar{\kappa}L \sim (L/\ell_e)^4$ as predicted by Brouzet *et al.* [12]. For long fibers ($L \gtrsim L_v$), the dissipated power is mainly due to the viscous dissipation due to the reconfiguration of the fiber. In that case, as long as the deformations are due to eddies whose size scales with the fiber length L, the mean curvature $\bar{\kappa}$ is expected to be given by

$$\rho L^3 \varepsilon \sim \frac{\eta L u_L}{\bar{\kappa}\tau_b}, \tag{27}$$

leading to

$$(\bar{\kappa}L)^3 \sim \frac{\rho L^{14/3}\varepsilon^{2/3}}{EI}. \tag{28}$$

Finally, by introducing L_v [see Eq. (3)] and the Kolmogorov length η_k, the normalized mean curvature scales as

$$\bar{\kappa}L \sim \left(\frac{L}{L_v}\right)^{10/9}\left(\frac{L}{\eta_k}\right)^{4/9}. \tag{29}$$

The spline used to compute the centerline creates artifacts that are amplified by the computation of the local curvature (second-order derivative of the position). Verifying this scaling law was out of the scope of this study, but some investigations will be done to accurately measure the local curvature. In this article, each time the notation $\bar{\kappa}L$ appears it corresponds, in fact, to the scaling (29).

The evolutions of the extents normalized by the fiber length L as a function of $\bar{\kappa}L$ are plotted in Fig. 6(b). The symbols correspond to experimental measurements and the red lines to the simple planar model where we have set $\bar{\kappa}L = 40\kappa_0$ to fit the experimental points. The measurements and the prediction are in very good agreement up to $\bar{\kappa}L \sim 60$. For longer fibers, the extents measured experimentally evolve less rapidly than the model. This suggests that the simple model of a planar conformation fails to reproduce our measurements. This is compatible with the previous observations from Gay *et al.* [14]. Indeed for very long fibers, the approximation of planar deformation no longer holds [see Fig. 6(b)]. In this regime, the eddies responsible for the local deformation can be smaller than the fiber length. Therefore, the expression of the mean curvature given in Eq. (29) does no longer hold and neither does the curvature profile we have considered in Eq. (17) (see Gay *et al.* [14] for more details).

V. CONCLUSION

To summarize, we have experimentally investigated the rotation of flexible fibers, straight at equilibrium, in a homogeneous and isotropic turbulent flow. The 3D reconstruction techniques have been validated by comparing the evolution of the end-to-end distance as a function of the flexibility of the fiber. Our measurements are overall in good agreement with the current literature. However, the influence of the Reynolds number might not be negligible contrary to what has been thought so far. We will return to this point later in the discussion. We then measured the rotation rates of both the end-to-end vector, as a proxy of the tumbling of the rigid fiber, and of the eigenframe of the fiber. We observed an increase of the tumbling rate when the fiber flexibility is increased. This feature can be captured by considering the mean end-to-end distance as the effective length of the fiber. More interestingly, the rotation of the eigenframe follows the same evolution as the tumbling rate of a rigid fiber when the lateral extents are considered. To model this observation we introduced a scaling for the evolution of the mean curvature for fibers whose length $L \gtrsim L_v$, which extends the previous scaling proposed by Brouzet *et al.* [12]. This scaling is valid as long as the deformations can be considered as planar.

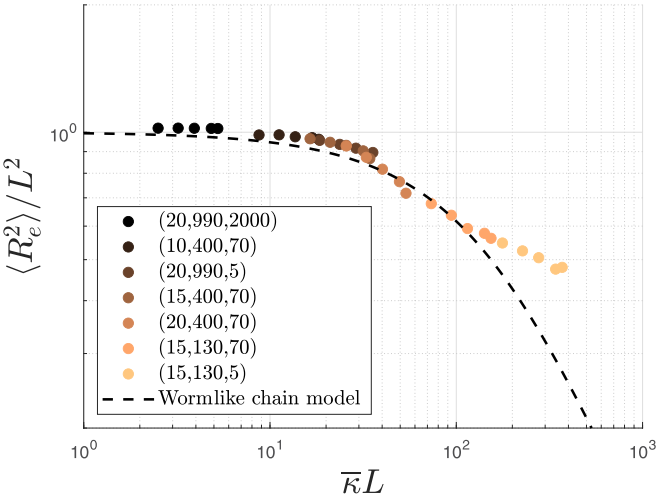


FIG. 7. Evolution of the normalized mean end-to-end distance as a function of the normalized mean curvature model (29). The dashed line represents the wormlike chain model where the persistence length is considered as $\overline{\kappa}^{-1}$.

Several additional questions are still open to understand the transport of flexible fibers in turbulence. Here we focus on the rotation rate of flexible fibers. Rosti *et al.* [15] showed that, in the underdamped regime, investigating the dynamics of the norm of the end-to-end vector gives access to the longitudinal structure function. In the overdamped regime, our study and the one from Gay *et al.* [14] show that a local deformation leads to a global reconfiguration of the fiber. One can then wonder whether the dynamics of the norm of the end-to-end vector can also be related to the structure function of turbulence in the overdamped regime. Similarly, it would be interesting to investigate the dynamics of the extents, which play a crucial role on the tumbling rate of a flexible fiber in turbulent flows.

A second important point is related to the mean curvature of the fibers $\bar{\kappa}L$, given in Eq. (29), which determines the evolution of the extents, and then of the rotation rate. This mean curvature also allows one to collapse the evolution of the mean end-to-end distance with the wormlike chain model as shown in Fig. 7. This suggests that the correlation length of the tangent vector is given by $\bar{\kappa}^{-1}$, and then that the mean curvature characterizes the amplitude of the deformation, contrary to the ratios L/ℓ_e or L/L_v, which characterize the regime of deformation (and $\bar{\kappa}$ depends on that regime). A full understanding of the transport of flexible fibers in turbulent flow requires then a better understanding of the evolution of the curvature in the different regimes both from a statistical and a dynamical point of view.

Finally, all the results presented here concern initially straight fibers. It might be interesting to investigate coiled fibers at rest. Indeed, as turbulence tends to stretch points apart [26], the influence of the deformation of these particles on their transport might be greater .

ACKNOWLEDGMENT

This work was carried out in the framework of NetFlex Project (ANR-21-CE30-0040) funded by the French National Research Agency (ANR).

DATA AVAILABILITY

The data that support the findings of this article are openly available [27].

[1] F. Lundell, L. D. Söderberg, and P. H. Alfredsson, Fluid mechanics of papermaking, Annu. Rev. Fluid Mech. **43**, 195 (2011).
[2] P. S. Ross, S. Chastain, E. Vassilenko, A. Etemadifar, S. Zimmermann, S.-A. Quesnel, J. Eert, E. Solomon, S. Patankar, A. M. Posacka, and B. Williams, Pervasive distribution of polyester fibres in the Arctic Ocean is driven by Atlantic inputs, Nat. Commun. **12**, 106 (2021).
[3] B. R. Sutherland, M. DiBenedetto, A. Kaminski, and T. van den Bremer, Fluid dynamics challenges in predicting plastic pollution transport in the ocean: A perspective, Phys. Rev. Fluids **8**, 070701 (2023).
[4] A. Pumir and M. Wilkinson, Orientation statistics of small particles in turbulence, New J. Phys. **13**, 093030 (2011).
[5] S. Parsa and G. A. Voth, Inertial range scaling in rotations of long rods in turbulence, Phys. Rev. Lett. **112**, 024501 (2014).
[6] T. B. Oehmke, A. D. Bordoloi, E. Variano, and G. Verhille, Spinning and tumbling of long fibers in isotropic turbulence, Phys. Rev. Fluids **6**, 044610 (2021).
[7] S. Brizzolara, M. E. Rosti, S. Olivieri, L. Brandt, M. Holzner, and A. Mazzino, Fiber tracking velocimetry for two-point statistics of turbulence, Phys. Rev. X **11**, 031060 (2021).
[8] M. Alipour, M. De Paoli, S. Ghaemi, and A. Soldati, Long non-axisymmetric fibres in turbulent channel flow, J. Fluid Mech. **916**, A3 (2021).
[9] V. Giurgiu, G. C. A. Caridi, M. De Paoli, and A. Soldati, Full rotational dynamics of plastic microfibers in turbulence, Phys. Rev. Lett. **133**, 054101 (2024).
[10] C. Marchioli, M. E. Rosti, and G. Verhille, Flexible fibers in turbulence, Annu. Rev. Fluid Mech. **58**, 167 (2026).
[11] C. Brouzet, G. Verhille, and P. Le Gal, Flexible fiber in a turbulent flow: A macroscopic polymer, Phys. Rev. Lett. **112**, 074501 (2014).
[12] C. Brouzet, R. Guiné, M.-J. Dalbe, B. Favier, N. Vandenberghe, E. Villermaux, and G. Verhille, Laboratory model for plastic fragmentation in the turbulent ocean, Phys. Rev. Fluids **6**, 024601 (2021).
[13] S. Olivieri, A. Mazzino, and M. E. Rosti, On the fully coupled dynamics of flexible fibres dispersed in modulated turbulence, J. Fluid Mech. **946**, A34 (2022).
[14] A. Gay, B. Favier, and G. Verhille, Characterisation of flexible fibre deformations in turbulence, Europhys. Lett. **123**, 24001 (2018).
[15] M. E. Rosti, A. A. Banaei, L. Brandt, and A. Mazzino, Flexible fiber reveals the two-point statistical properties of turbulence, Phys. Rev. Lett. **121**, 044501 (2018).
[16] S. Bounoua, G. Bouchet, and G. Verhille, Tumbling of inertial fibers in turbulence, Phys. Rev. Lett. **121**, 124502 (2018).
[17] G. Verhille, Deformability of discs in turbulence, J. Fluid Mech. **933**, A3 (2022).
[18] R. Hartley and A. Zisserman, *Multiple View Geometry in Computer Vision* (Cambridge University Press, Cambridge, UK, 2004).
[19] G. Verhille and A. Bartoli, 3D conformation of a flexible fiber in a turbulent flow, Exp. Fluids **57**, 117 (2016).
[20] H. M. De La Rosa Zambrano, G. Verhille, and P. Le Gal, Fragmentation of magnetic particle aggregates in turbulence, Phys. Rev. Fluids **3**, 084605 (2018).
[21] J. Hoschek and D. Lasser, *Fundamentals of Computer-Aided Geometric Design* (A.K. Peters, Wellesley, Massachusetts, USA, 1993).
[22] G. Farin, *Curves and Surfaces for Computer Aided Geometric Design: A Practical Guide* (Academic, Cambridge, 1997).
[23] M. Sulaiman, E. Climent, B. Delmotte, P. Fede, F. Plouraboué, and G. Verhille, Numerical modeling of long flexible fibers in homogeneous isotropic turbulence, Eur. Phys. J. E **42**, 132 (2019).
[24] O. Kratky and G. Porod, Diffuse small-angle scattering of x-rays in colloid systems, J. Colloid Sci. **4**, 35 (1949).
[25] T. R. Powers, Dynamics of filaments and membranes in a viscous fluid, Rev. Mod. Phys. **82**, 1607 (2010).
[26] C. Meneveau, Lagrangian dynamics and models of the velocity gradient tensor in turbulent flows, Annu. Rev. Fluid Mech. **43**, 219 (2011).
[27] https://doi.org/10.57745/WRJTJR.